

The Eclipsing Binaries from the LAMOST Medium-resolution Survey.III. A High-precision Empirical Stellar Mass Library

JIANPING XIONG,^{1,2} CHAO LIU^{†, 3, 4, 2} JIAO LI,³ JIADONG LI,^{3, 2} BO ZHANG,³ XIAODIAN CHEN,^{5, 6, 7} CHANGQING LUO,³
 ZIHUANG CAO,^{1, 6} AND YONGHENG ZHAO^{1, 6}

¹*Key Laboratory of Optical Astronomy, National Astronomical Observatories, Chinese Academy of Sciences
 Beijing 100101, China*

²*University of Chinese Academy of Sciences
 Beijing 100049, China*

³*Key Laboratory of Space Astronomy and Technology, National Astronomical Observatories, Chinese Academy of Sciences
 Beijing 100101, China*

⁴*Institute for Frontiers in Astronomy and Astrophysics, Beijing Normal University, Beijing, 102206, China*

⁵*Key Laboratory of Optical Astronomy, National Astronomical Observatories, Chinese Academy of Sciences,
 Beijing 100101, China*

⁶*School of Astronomy and Space Science, University of the Chinese Academy of Sciences, Beijing 101408, China*

⁷*Department of Astronomy, China West Normal University, Nanchong, China*

ABSTRACT

High-precision stellar mass and radius measured directly from binaries can effectively calibrate the stellar models. However, such a database containing full spectral types and large range of metallicity is still not fully established. A continuous effort of data collecting and analysis are requested to complete the database. In this work, we provide a catalog containing 184 binaries with independent atmospheric parameters and accurate masses and radii as the benchmark of stellar mass and radius. The catalog contains 56 new detached binaries from LAMOST Medium-resolution spectroscopic (MRS) survey and 128 detached eclipsing binaries compiled from previous studies. We obtain the orbital solutions of the new detached binaries with uncertainties of masses and radii smaller than 5%. These new samples densify the distribution of metallicity of the high-precision stellar mass library and add 9 hot stars with $T_{\text{eff}} > 8000$ K. Comparisons show that these samples well agree with the PARSEC isochrones in $T_{\text{eff}} \text{-} \log g$ -mass-radius-luminosity space. We compare mass and radius estimates from isochrone and SED fitting, respectively, with those from the binary orbital solution. We find that the precision of the stellar-model dependent mass estimates is $> 10\%$ and the precision of the radius estimates based on atmospheric parameters is $> 15\%$. These give a general view of the uncertainty of the usual approaches to estimate stellar mass and radius.

Keywords: Stellar masses(1614)—Detached binary stars(375) — Astronomy data analysis(1858) — Astronomy databases(83) — Catalogs(205)

1. INTRODUCTION

Stars, as the main ingredient of galaxies, play critical role in the structure and evolution of galaxies. An accurate understanding of their mass, radius, luminosity, chemical composition, and age is therefore an essential task. In general, The stellar mass and radius

can be mainly derived from the stellar structure and evolution models, e.g. PARSEC (Bressan et al. 2012), Y^2 (Demarque et al. 2004, 2008), Dartmouth (Dotter et al. 2008), MIST (Dotter 2016) etc., empirical relations, e.g. mass-luminosity relation (MLR), mass-radius relation (MRR), and mass-temperature relation (MTR) (Eker et al. 2014, 2015, 2018), or asteroseismic techniques (Marcy et al. 2014; Chaplin et al. 2014). Among these methods, dynamical mass of the detached eclipsing binaries is not only the method that minimally relies on stellar models, but also reaches precision of around

Corresponding author: Chao Liu
 liuchao@nao.cas.cn

1% (Torres et al. 2010). Therefore, it can be used as calibrator for the other mass estimation approaches. Indeed, most of the stellar models and empirical relations rely on the dynamical masses and radii for calibration (Cox 2000; Hoxie 1973; Torres et al. 2010; Southworth 2015; Eker et al. 2015, 2018).

However, by now, only ~ 700 binaries are provided with accurate masses and radii. Among them, only < 200 binary systems have the comprehensive atmospheric parameters (T_{eff} , $\log g$, [M/H]). Metallicity is the especially important parameter accompany with stellar mass and radius, since it can help to break the mass-metallicity degeneracy at around turn-off point (Serenelli et al. 2021). With metallicity, one can derive the luminosity-mass and other relations for different metallicity so that the empirical mass can be well compared with stellar models.

It is clear that enlarging the dataset of stars with accurate stellar mass and metallicity can significantly improve the calibration of the stellar models. Recently, significant progress has been made in spectroscopic surveys, e.g. RAVE (Steinmetz et al. 2006, 2020), SDSS/SEGUE (Yanny et al. 2009), LAMOST (Cui et al. 2012; Deng et al. 2012; Zhao et al. 2012; Luo et al. 2015), APOGEE (Majewski et al. 2017), and GALAH (De Silva et al. 2015) and time-domain photometric surveys, e.g. Gaia (Gilmore et al. 2012; Katz et al. 2004; Cropper et al. 2018), NASA/Kepler (Borucki et al. 2010; Batalha et al. 2010; Abdul-Masih et al. 2016), TESS (Ricker et al. 2015), ZTF (Bellm et al. 2019), and ASAS-SN (Kochanek et al. 2017; Jayasinghe et al. 2019).

In particular, LAMOST has launched a medium-resolution survey (MRS, $R \sim 7500$), which includes both time-domain and usual spectroscopic observations (Liu et al. 2020), since October 2018. Moreover, relatively high-quality parameters from the spectra have been obtained. For LAMOST low-resolution spectra (LRS with $R \sim 1800$), the accuracy of radial velocity, T_{eff} , $\log g$ and [Fe/H] are around 5 km s^{-1} , 150 K , 0.25 dex , and 0.15 dex , respectively (Xiang et al. 2015). For LAMOST MRS, the accuracy of radial velocity can reach around 1 km s^{-1} (Wang et al. 2019; Zhang et al. 2021; Xiong et al. 2021). The accuracy of T_{eff} , $\log g$, and [Fe/H] are around 119 K , 0.17 dex , and $0.06 \sim 0.12 \text{ dex}$, respectively (Wang et al. 2020). Furthermore, many eclipsing binaries with light curves (Slawson et al. 2011; Jayasinghe et al. 2021; Chen et al. 2020) are identified from LAMOST survey (Li et al. 2021a; Zhang et al. 2022). These published data offer a unique opportunity to measure the dynamic mass and radius of more eclipsing binaries.

This work aims to present a high-precision empirical stellar mass library that includes the accurate dynamical mass and the independently measured atmospheric parameters (T_{eff} , $\log g$, [M/H]) from observed spectra for main-sequence stars. The literature data compilation and LAMOST data acquisition and light curve are described in Section 2. The method of measuring accurate mass for LAMOST binaries is described in Section 3. The results are indicated in Section 4. The comparison of dynamical mass and radius derived from different measurement approaches is discussed in Section 5. Finally, we summarize in Section 6.

2. DATA

2.1. Literature data compilation

Although previous studies have already published ~ 700 binary systems with accurate stellar mass and radius (Torres et al. 2010; Southworth 2015; Eker et al. 2015, 2018; Dieterich et al. 2021), we can only make use of < 200 samples with comprehensive atmospheric parameters (T_{eff} , $\log g$, [M/H]) among the full dataset to provide masses and radii in different metallicity. We select the samples from literature under the following criteria: 1) the binaries are composed of two main-sequence companions; 2) the masses and radii are estimated from binary orbital dynamics, and 3) T_{eff} , $\log g$, and [M/H] of (at least) the primary stars are independently derived from spectroscopic data. We finally obtained 128 binaries, 19 from Torres et al. (2010), 78 from Southworth (2015), 24 from Eker et al. (2018), 5 from Dieterich et al. (2021), and the remaining 2 from Wang et al. (2021) and Pan et al. (2020), respectively. These data have the uncertainties of the mass and radius estimates at around $1 \sim 2\%$. Their metallicity precision is as high as about 0.05 dex.

These samples are still not sufficient if we want to demonstrate the mass-luminosity relation and other important relations in a large range of effective temperature at different metallicity. Therefore, we need to extend the sample based on the LAMOST survey data.

2.2. LAMOST data with light curves

LAMOST is a 4-meter class reflective Schmidt telescope with a 5-degree field-of-view. Totally, 4000 fibers are installed at its 1.75 m -diameter focal plane. These fibers go into 16 spectrographs, each of which accepts 250 fibers so that it can take the spectra of 4,000 targets simultaneously. At resolution of $R \sim 1800$, LAMOST reaches about $r \sim 18 \text{ mag}$ with 1.5-hour exposure. As October 2018, LAMOST has started the 5-year medium-resolution spectroscopic (MRS) survey ($R \sim 7500$ with limiting magnitude of $G < 15 \text{ mag}$), which includes a

time-domain spectroscopic survey sub-project. It is expected that, after a 5-year MRS survey, more than a hundred thousands stars will be observed with ~ 60 exposures (Liu et al. 2020). This provides a unique opportunity to collect a larger sample of binary stars with their orbits resolved.

The uncertainty of radial velocities of LAMOST MRS spectra is around 1 km s^{-1} for late-type stars (Wang et al. 2019; Zhang et al. 2021; Xiong et al. 2021), the stellar atmospheric parameters (T_{eff} and $\log g$) and 13 chemical abundances are derived for LAMOST MRS by a deep-learning method with uncertainties of 119 K , 0.17 dex , and $0.06\text{--}0.12 \text{ dex}$ for T_{eff} , $\log g$, and elemental abundances, respectively (Wang et al. 2020). As expected, the rotation of the stars can also be determined under uncertainty of 10 km s^{-1} . For LAMOST LRS, LSP3 can achieve an accuracy of 5 km s^{-1} , 150 K , 0.25 dex , and 0.15 dex for radial velocity, T_{eff} , $\log g$, and [Fe/H], respectively (Xiang et al. 2015).

We initially identified 1502 EA-type eclipsing binaries with both LAMOST DR8 MRS multi-epoch spectra and light curves from Kepler eclipsing binary catalog (Prša et al. 2011), ZTF Data Release 2 (Chen et al. 2020), and ASAS-SN catalog (Jayasinghe et al. 2020). Then the following criteria are used to select high quality samples:

- 1) the double-line spectroscopic binaries are selected;
- 2) the binaries with at least 30 exposures with signal-to-noise ratio larger than 10 are selected;
- 3) atmospheric parameters of primary stars have been measured at the time of secondary minimum (when the primary star obscures the secondary star).

Finally, we select 56 systems from LAMOST DR8 MRS and further estimate the masses and radii by resolving their orbital solutions. Their radial velocity velocity curves were derived by Zhang et al. (2021) via LAMOST multiple-epoch spectra.

3. METHOD

3.1. Brief description

For each star, the light curve with eclipses and the radial velocity curves of two companions covering the whole period are ready to derive the orbital solution. Light curves with eclipses are able to constrain the inclination and relative radii of both companions with respect to the semi-major axis (R/a). However, the stellar mass cannot be solely determined without double-line radial velocity curves. In this subsection we describe the general method to derive the stellar masses and radii of two companions in a binary system via the orbital solution.

The radial velocity of any of the companions in a spectroscopic binary system can be written as

$$RV_i = \frac{2\pi a_i \sin i}{P(1 - e^2)^{1/2}} [\cos(\theta + \omega) + e \cos \omega] + \gamma, \quad (1)$$

where P is the orbital period, θ is the angular position, ω is the longitude of the periastron, e is the orbital eccentricity, a_i is the semi-major distance from the i th companion to the barycenter, i is the inclination of orbit, and γ is the systematic velocity. The coefficient of the right-hand side is actually the semi-amplitude of the radial velocity curve and is usually denoted as

$$\begin{aligned} K_1 &= \frac{2\pi a_1 \sin i}{P(1 - e^2)^{1/2}}, \\ K_2 &= \frac{2\pi a_2 \sin i}{P(1 - e^2)^{1/2}}. \end{aligned} \quad (2)$$

K_i and P are associated with the stellar masses via the mass function, which can be written as

$$\begin{aligned} f(M_1) &= \frac{M_1^3 \sin^3 i}{(M_1 + M_2)^2} \\ &= (1.0361 \times 10^{-7})(1 - e^2)^{3/2} K_2^3 P \quad M_{\odot}, \\ f(M_2) &= \frac{M_2^3 \sin^3 i}{(M_1 + M_2)^2} \\ &= (1.0361 \times 10^{-7})(1 - e^2)^{3/2} K_1^3 P \quad M_{\odot}. \end{aligned} \quad (3)$$

Although the radial velocity curves can give K_1 and K_2 , they cannot directly solve M_1 and M_2 without the help of light curves.

We then seek the orbit solution with the combination of the radial velocities and light curves using PHysics Of Eclipsing BinariEs (PHOEBE 2.2¹; Prša & Zwitter 2005; Prša et al. 2016; Jones et al. 2020), which is based on the WD code (Wilson & Devinney 1971).

The atmospheric parameters of the F, G, and K type stars among the 56 stars are from the LAMOST pipeline (Wu et al. 2014), while those of the M dwarf and OB type stars are from Li et al. (2021b) and Guo et al. (2021), respectively. For the secondary star, the T_{eff} , $\log g$ are resulted by the best orbit fitting from PHOEBE.

In this work, the effective temperature and $\log g$ of the primary stars are estimated from the spectra observed near the secondary minimum eclipse, at which the secondary stars give minimum contribution in fluxes. As an instance, the secondary only contributes about 11% of the primary fluxes near the secondary minimum eclipse when $q=0.7$ (El-Badry et al. 2018). These parameters are then dominated by primary stars and used as inputs in PHOEBE for orbit solution.

¹ <http://phoebe-project.org>

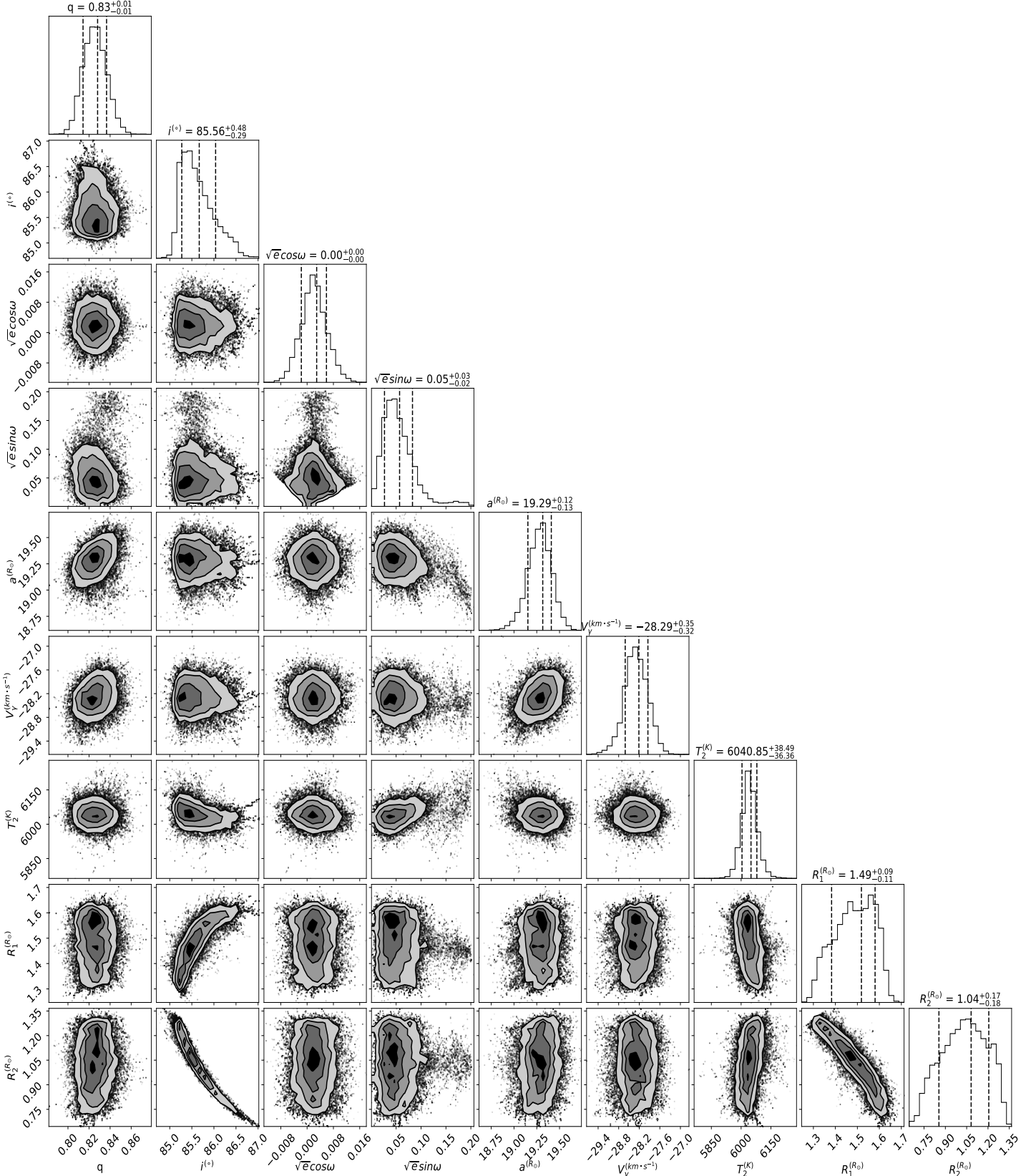


Figure 1. As a sample of the orbital solution, this figure shows the MCMC derived the probability density function of the orbital parameters for KIC 5359678 (Wang et al. 2021). From left column to the right, the histograms are for q , i , $\sqrt{e}\cos\omega$, $\sqrt{e}\sin\omega$, a , V_γ , T_2 , R_1 , and R_2 .

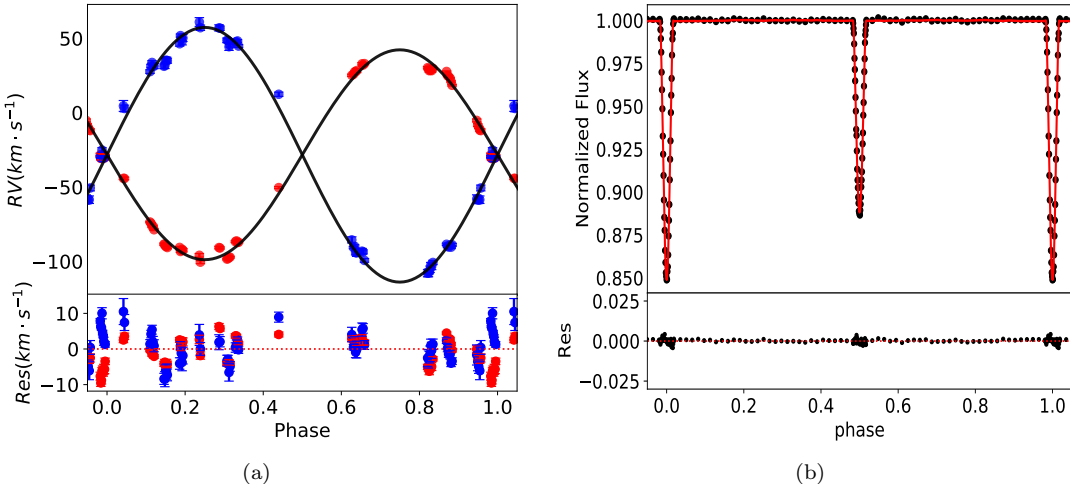


Figure 2. Panel (a): The radial velocity curves. In the top panel, the red and blue dots are the observed radial velocities of KIC 5359678 (Wang et al. 2021). The best-fit result derived by PHOEBE is shown with black solid lines. The bottom panel shows the residuals of radial velocities between the model and observations. Panel (b): The top panel shows the light curves for KIC 5359678 with black dots. The red solid line represent for the best-fit model derived by PHOEBE. The bottom panel shows the residuals between model and observations.

El-Badry et al. (2018) performed experiments with synthetic spectra to investigate the systematic biases of atmospheric parameters for unresolved main-sequence binaries on spectral fitting with single star models, they modeled spectra similar to those collected by the APOGEE, GALAH and LAMOST surveys. They found that, when an unresolved binary was considered as a single star, the typical errors of T_{eff} , $\log g$ and [Fe/H] estimates from the combined spectra are <200 K, <0.1 dex and <0.1 dex for LAMOST low-resolution spectra. These systematic errors are analog to the measurement error and hence would not significantly affect the final results of the mass and radius estimation.

A Markov chain Monte Carlo (MCMC²; Foreman-Mackey et al. 2013) sampling is then applied on PHOEBE to solve out all orbital parameters. The likelihood used in the MCMC is a joint chi-square value from the residuals of the fits with the observational light curve and radial velocity curves. The following priors are also added to restrict the MCMC sampling:

1. mass ratio (q): $0 < q < 2$
 2. orbit inclination (i°): $0 < i < 90^\circ$
 3. eccentricity (e): $0 < e < 1$
 4. argument of periastron (ω°): $0 < \omega < 360^\circ$
 5. semi-major of orbit (a): $0 < a/R_\odot < 100$
 6. system velocity (V_γ :): $-200 < V_\gamma/(\text{km s}^{-1}) < 200$
 7. effective temperature of secondary (T_2): $3000 < T_2/\text{K} < T_2 + 3\sigma_{T_1}$

8. equivalent radius of primary (R_1): $0 < R_1/R_\odot < 10$
 9. equivalent radius of secondary (R_2): $0 < R_2/R_\odot < 10$

We initialized the chains of MCMC using random values drawn from uniform distributions with the restricting ranges defined above. The surface gravity and reflection coefficient are fixed in PHOEBE unless the T_{eff} of the primary star is larger than $8000 K$. For each star, we run the model with 80 walkers, each of which takes 2000 steps. Finally, we calculate the peak value of the probability distribution and the standard deviations of the random drawn points as the best-fit parameters and their uncertainties.

3.2. Method verification

As a verification of the method, we solve out the orbit for KIC 5359678 and compare with the results with (Wang et al. 2021). Figure 1 shows our MCMC result for KIC 5359678. In the corner plot, each histogram shows the probability distributions of q , i , $\sqrt{e}\cos\omega$, $\sqrt{e}\sin\omega$, a , V_γ , T_2 , R_1 and R_2 .

Figure 2 (a) shows the observed and the best-fit radial velocity curve. The residuals of the velocity indicate that the uncertainty of the best-fit radial velocity curve is around 4.24 km s^{-1} . The top of panel (b) shows the best-fit light curve model by PHOEBE (red line) and the corresponding light observation (black dots), and the bottom of the panel shows the residuals of the light curve between the model fit and observations. It illustrates that the best-fit radial velocity curves model and light curve well match with the observed data.

² <http://dan.iel.fm/emcee>

Table 1. Comparison of the orbital parameters of KIC 5359678 between this work and Wang et al. (2021).

Parameters	(Wang et al. 2021)	This work	Parameters	(Wang et al. 2021)	This work
e	0.00032 ± 0.00006	0.0024 ± 0.0057	$T_2(K)$	5980 ± 22	6040.84 ± 40.75
$\omega^a (\circ)$	-89.55 ± 1.05	88.00 ± 6.03	$M_1(M_\odot)$	1.320 ± 0.060	1.361 ± 0.008
$i (\circ)$	85.56 ± 0.10	85.56 ± 0.37	$M_2(M_\odot)$	$1.12 \pm$	1.121 ± 0.008
q	0.851 ± 0.10	0.825 ± 0.011	$R_1(R_\odot)$	1.52 ± 0.04	1.490 ± 0.080
$V_\gamma (\text{km s}^{-1})$	-29.26 ± 0.19	-28.29 ± 0.34	$R_2(R_\odot)$	1.05 ± 0.05	1.075 ± 0.130
$a(R_\odot)$	19.19	19.28 ± 0.13	$\log g$	-	4.200 ± 0.079
$T_1(K)$	6500 ± 50	6501.04 ± 47.94	$[M/H]$	-	-0.104 ± 0.046

^aWang et al. (2021) derived ω by $\text{ecos}\omega = \pi/2[(\phi_2 - \phi_1) - 0.5]$, and $\text{esin}\omega = (w_2 - w_1)/(w_2 + w_1)$. ϕ_2 is the phase of the secondary eclipses, $\phi_1 = 0$, w_1 and w_2 are widths of primary and secondary eclipse in phase, respectively (Kjurkchieva & Vasileva 2015).

Table 2. List of 10 of the samples compiled from previous studies with accurate masses, radii, and atmospheric parameters (T_{eff} , $\log g$, $[M/\text{H}]$)

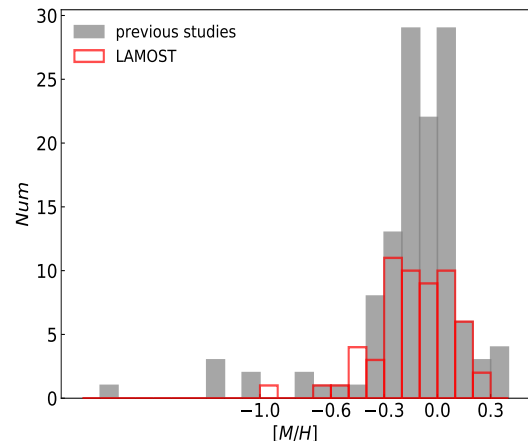
Name	T_{eff} [K]	$\log g$ [dex]	$[M/\text{H}]$ [dex]	$\log L/L_\odot$	$M [M_\odot]$	$R [R_\odot]$	Ref.
47 Tuc E32	6025.60 ± 18.08	4.227 ± 0.002	-0.71 ± 0.10	0.221 ± 0.012	0.862 ± 0.002	1.183 ± 0.001	(Thompson et al. 2020)
	5956.62 ± 17.87	4.352 ± 0.003	-0.71 ± 0.10	0.059 ± 0.012	0.827 ± 0.002	1.004 ± 0.002	
47 Tuc V69	5956.62 ± 17.86	4.143 ± 0.003	-0.71 ± 0.1	0.293 ± 0.012	0.876 ± 0.002	1.315 ± 0.002	(Thompson et al. 2020)
	5984.12 ± 17.95	4.242 ± 0.003	-0.71 ± 0.10	0.193 ± 0.013	0.859 ± 0.003	1.162 ± 0.003	
AD Boo	6575.0 ± 120.0	4.173 ± 0.008	0.10 ± 0.15	0.642 ± 0.075	1.414 ± 0.008	1.613 ± 0.014	(Clausen et al. 2008)
	6145.0 ± 120.0	4.350 ± 0.007	0.10 ± 0.15	0.279 ± 0.080	1.209 ± 0.006	1.216 ± 0.010	
AH Cep	30690.22 ± 245.52	4.019 ± 0.012	0.0 ± 0.0	4.530 ± 0.034	16.140 ± 0.113	6.510 ± 0.044	(Popper & Hill 1991)
	28773.98 ± 230.19	4.073 ± 0.018	0.0 ± 0.0	4.294 ± 0.036	13.690 ± 0.092	5.640 ± 0.048	
AI Phe	5010.0 ± 120.0	3.595 ± 0.014	-0.14 ± 0.10	0.689 ± 0.101	1.234 ± 0.005	2.932 ± 0.048	(Andersen et al. 1988)
	6310.0 ± 150.0	3.996 ± 0.011	-0.14 ± 0.10	0.674 ± 0.098	1.193 ± 0.004	1.818 ± 0.024	
AL Ari	6367.95 ± 25.47	4.229 ± 0.005	-0.42 ± 0.08	0.446 ± 0.017	1.164 ± 0.001	1.372 ± 0.004	(Graczyk et al. 2021)
	5559.04 ± 27.80	4.458 ± 0.008	-0.42 ± 0.08	-0.152 ± 0.021	0.911 ± 0.000	0.905 ± 0.003	
AL Dor	6053.41 ± 30.27	4.404 ± 0.002	-0.10 ± 0.04	0.159 ± 0.020	1.102 ± 0.000	1.092 ± 0.001	(Gallenne et al. 2019)
	6053.41 ± 30.27	4.399 ± 0.002	-0.10 ± 0.04	0.164 ± 0.020	1.103 ± 0.000	1.098 ± 0.001	
ASAS J045021+2300.4	5662.39 ± 28.31	4.360 ± 0.018	-0.26 ± 0.26	0.016 ± 0.027	0.934 ± 0.007	1.058 ± 0.010	(Hełminiak et al. 2021)
	3589.22 ± 43.07	4.829 ± 0.019	-0.26 ± 0.26	-1.604 ± 0.052	0.409 ± 0.002	0.408 ± 0.004	
ASAS J051753-5406.0	5984.12 ± 89.76	3.982 ± 0.006	-0.1 ± 0.13	0.636 ± 0.061	1.311 ± 0.015	1.935 ± 0.009	(Miller et al. 2022)
	5847.90 ± 81.87	4.332 ± 0.008	-0.1 ± 0.13	0.167 ± 0.057	1.093 ± 0.013	1.181 ± 0.006	
ASAS J052821+0338.5	5105.05 ± 45.95	4.05 ± 0.01	-0.15 ± 0.14	0.312 ± 0.036	1.375 ± 0.005	1.830 ± 0.004	(Stempels et al. 2008)
	4709.77 ± 42.39	4.08 ± 0.01	-0.15 ± 0.14	0.123 ± 0.036	1.329 ± 0.003	1.730 ± 0.004	

The masses and radii of the primary and secondary of KIC5359678 that we obtain from PHOEBE with MCMC are $M_1 = 1.361 \pm 0.008 M_\odot$, $R_1 = 1.49 \pm 0.08 R_\odot$, $M_2 = 1.121 \pm 0.008 M_\odot$, $R_2 = 1.075 \pm 0.130 R_\odot$. All best-fit parameters of the MCMC and those obtained by (Wang et al. 2021) are listed and compared in Table 1. It illustrates that the orbital parameters obtained with PHOEBE+MCMC are consistent with those by Wang et al. (2021) within the uncertainties.

4. RESULTS

We compile 128 detached binary systems with atmospheric parameters and accurate masses and radii. The 10 of 128 detached eclipsing binaries are presented in table 2, the whole catalog can be found in China-VO: doi:10.12149/101147.

In table 3, the masses, radii, and atmospheric parameters of 58 double-line eclipsing binaries selected from

**Figure 3.** The [M/H] distribution of sample stars compiled in this work.

LAMOST MRS are displayed. It contains 56 new or-

Table 3. Summary of 10 of binary samples obtained from LAMOST MRS with the masses, radii, and atmospheric parameters (T_{eff} , $\log g$, [M/H]).

No.	gaia_source_id	T_{eff} [K]	$\log g$ [dex]	$\log L/L_{\odot}$	M [M_{\odot}]	R [R_{\odot}]	[M/H] [dex]	$v \sin i$ [km s $^{-1}$]
1 ^a	2101510803402761344	6500.00±50.00	4.200±0.079	0.570±0.061	1.320±0.060	1.520±0.040	-0.104±0.046	79.310
		5980.00±22.00	4.544±0.070	0.104±0.096	1.120±0.000	1.050±0.050	-0.104±0.046	-
2 ^b	2126356983051726720	6144.00±100.00	4.220±0.010	0.431±0.066	1.290±0.020	1.450±0.010	-0.019±0.035	288.310
		5966.00±97.00	4.330±0.020	0.216±0.067	1.110±0.050	1.200±0.010	-0.019±0.035	-
3	2101192082470870912	6012.74±23.74	4.105±0.022	0.413±0.144	1.208±0.003	1.482±0.106	0.142±0.014	89.190
		5767.75±21.55	3.985±0.051	0.559±0.088	1.281±0.003	1.905±0.083	0.142±0.014	-
4	3811041442290209024	5940.85±32.41	4.157±0.053	0.237±0.164	1.065±0.031	1.240±0.101	-0.303±0.031	54.630
		4482.10±131.76	3.547±0.080	0.463±0.222	1.027±0.031	2.824±0.266	-0.303±0.031	-
5	3423803170795356800	16074.66±100.00	3.656±0.300	2.838±0.059	3.452±0.044	3.384±0.091	-0.350±0.100	-
		16186.85±200.69	4.019±0.100	2.724±0.143	3.272±0.044	2.927±0.197	-0.350±0.100	-
6	3378228658638299136	9824.11±1000.00	3.659±0.100	1.676±0.423	2.137±0.060	2.375±0.136	-0.482±0.100	-
		9423.69±249.40	4.024±0.121	1.544±0.218	1.901±0.060	2.219±0.211	-0.482±0.100	-
7	604716006409635456	5529.74±45.16	4.210±0.100	0.238±0.320	1.594±0.013	1.432±0.228	0.030±0.130	66.400
		6598.67±519.58	4.000±0.238	0.826±0.506	1.432±0.013	1.980±0.392	0.030±0.130	-
8	598940203109496064	4697.68±43.23	4.130±0.200	-0.717±0.254	0.746±0.011	0.661±0.083	-0.224±0.170	-
		4658.78±123.60	4.434±0.260	-0.490±0.410	0.756±0.011	0.873±0.173	-0.224±0.170	-
9	609180023619173632	5971.97±10.79	3.800±0.040	0.696±0.101	1.148±0.009	2.081±0.105	-0.234±0.010	126.360
		5665.94±84.29	3.836±0.078	0.633±0.161	1.157±0.009	2.150±0.161	-0.234±0.010	-
10	658309364243893504	5840.19±128.78	3.972±0.107	0.688±0.311	0.825±0.030	2.156±0.322	0.034±0.067	83.920
		5343.71±240.28	3.770±0.153	0.468±0.378	0.859±0.030	1.998±0.332	0.034±0.067	-

^a (Wang et al. 2021)

^b (Pan et al. 2020)

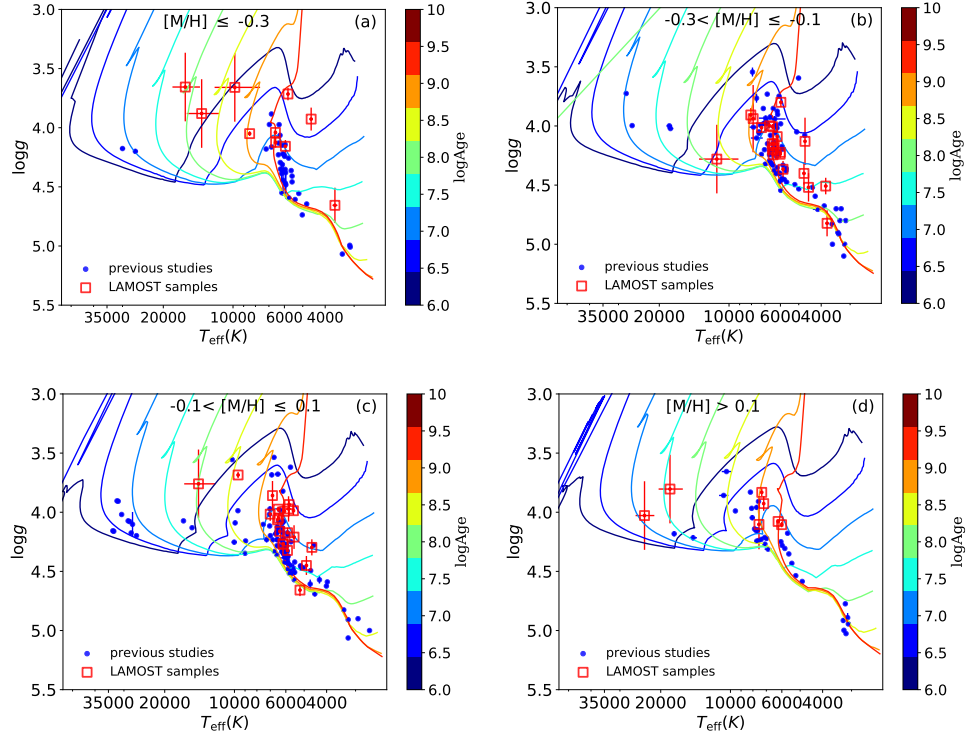


Figure 4. The (T_{eff} - $\log g$) diagram of samples. From left to right and top to bottom, the panels display the samples with $[\text{M}/\text{H}] \leq -0.3$, $-0.3 < [\text{M}/\text{H}] \leq -0.1$, $-0.1 < [\text{M}/\text{H}] \leq +0.1$, and $[\text{M}/\text{H}] > +0.1$, respectively. The blue dots are the samples compiled from the literature and the red rectangles are the samples from LAMOST MRS. The lines are the isochrones given by PARSEC models (Bressan et al. 2012) with color-coded ages ranging from 10 Myr to 10 Gyr.

bital solutions of binaries. In table 3, we also provide

the parameters of secondary stars obtained from orbital

solution with PHOEBE. Although the internal errors of the parameters of the secondary stars are similar to those of the primary, T_{eff} and $\log g$ may be have larger uncertainty in the measurement.

In this work, a total of 128 binaries with dynamic masses, radii, T_{eff} , $\log g$, and [M/H] are compiled, including 128 binaries composed of two main-sequence stellar companions from literature data and 56 new orbited solutions of binaries from LAMOST DR8 MRS. Figure 3 shows the [M/H] distribution of these stars. The range of [M/H] is between -1.86 dex to 0.61 dex. The filled histogram is the [M/H] distribution of samples from literature, while the red hollow histogram indicates the distribution of the samples from LAMOST DR8 MRS. It is seen that, while most of the LAMOST samples are concentrated around the solar metallicity, similar to the previous samples, a few of them locating at lower metallicity help to densifying the distribution of metallicity.

Figure 4 shows the $T_{\text{eff}}-\log g$ relation of the stars in different [M/H] bins. Most of the samples are in the main-sequence stage. At the temperature around 6000 K, some older stars just about to move away from the main-sequence and show the turn-off point. The red rectangles show that the new LAMOST samples well fill up with the metal-poor regime (see the top-left panel). Meanwhile, because the hot stars are more sensitive to the age, the new LAMOST samples also provide more sampling point at different ages in the regime of high T_{eff} .

4.1. Comparison with PARSEC

4.1.1. $T_{\text{eff}}-M$ relations in different ranges of [M/H]

Figure 5 shows the $T_{\text{eff}}-M$ relation of the samples. The samples cover a temperature range from 2600 to 38 000 K. In panel (a), the solid lines indicate the zero age main-sequence (ZAMS) with color-coded [M/H] from PARSEC model. Although the model isochrones show metallicity difference in $T_{\text{eff}}-M$ plane, the stellar samples overlapped with the isochrones do not show clear gradient in metallicity with $T_{\text{eff}} > 6000$ K. This is likely caused by the relatively smaller difference in mass and T_{eff} than the measurement uncertainties of the two parameters. However, for the stars with $T_{\text{eff}} < 6000$ K, it seems that the metallicity gradient can be seen in the observed samples. The orange and red dots, which represent for high metallicity, are located on top of the bluish symbols, which stand for the low metallicity stars.

We separately show the $T_{\text{eff}}-M$ relationships at different metallicity bins, as shown from panel (b) to (e), so that detailed comparison between the PARSEC model and the observed stars can be made.

It is seen that most of the stars are well consistent with the stellar models except for the cold stars with $T_{\text{eff}} < 5000$ K. The cold, low-mass stars show a steeper slope than the stellar models (dashed lines in the panels) in the variation of the stellar mass when T_{eff} declines. This implies that the mass directly estimated from the effective temperature of these cold stars may be over-estimated when $M \sim 0.1 M_{\odot}$ and under-estimated when $M \sim 0.5 M_{\odot}$. Although such systematic may only around a few hundredth M_{\odot} , it may potentially flatten the slope of the initial mass function.

Nevertheless, figure 5 implies that the effective temperature combined with a quite coarse estimation of metallicity can approximate the stellar mass in a quite robust way. Therefore, we provide an empirical polynomial model of the stellar mass depending on T_{eff} and [M/H]. It is not trivial to fit the mass as a function of T_{eff} and [M/H] with totally free constraints in the coefficients of a polynomial. Hence, we firstly fit a quartic polynomial to the stellar model and then fix the coefficients of the 3rd and 4th order terms of $\log T_{\text{eff}}$ obtained from the first step and fit the rest coefficients to the data. After a few tests, we adopt the following form of the quartic polynomial

$$\log(M) = a_1 + a_2 \log(T) + a_3 \log(T)^2 + 18.398 \log(T)^3 - 0.998 \log(T)^4 + a_4 Z, \quad (4)$$

where T and Z represent for T_{eff} and [M/H]. The best-fit a_1 , a_2 , a_3 , a_4 are 414.761, 372.928, -124.902, 12.088, respectively. It is noted that the relationship derived among these various parameters only apply for unevolved stars. The gray solid lines in the panels (b)-(e) indicate the best-fit polynomial model. The relative residuals showing at the bottom of panels (b)-(e) are around 11~18%.

In panel (b), benefited from the observation of lower metallicity stars in the outer disk of the Milky Way by LAMOST, we can see that there is an extension at the part of high T_{eff} .

In panels (c) and (d), which correspond to $-0.3 < [\text{M}/\text{H}] \leq -0.1$ and $-0.1 < [\text{M}/\text{H}] \leq +0.1$, the numbers of samples from LAMOST fill some vacancies in T_{eff} so that the coverage of T_{eff} becomes more continuous. In panel (e), for the stars with $[\text{M}/\text{H}] > +0.1$, the LAMOST samples also extend the range of T_{eff} to higher value.

4.1.2. $T_{\text{eff}}-R$ relations in different ranges of [M/H]

Figure 6 shows the $T_{\text{eff}}-R$ relation of the samples. Similar to figure 5, we draw the relation for the whole stars in panel (a) and those for different metallicity ranges in the rest four panels. Unlike $T_{\text{eff}}-M$ relation, $T_{\text{eff}}-R$ relation depends on the age of stars. Therefore, the stars in

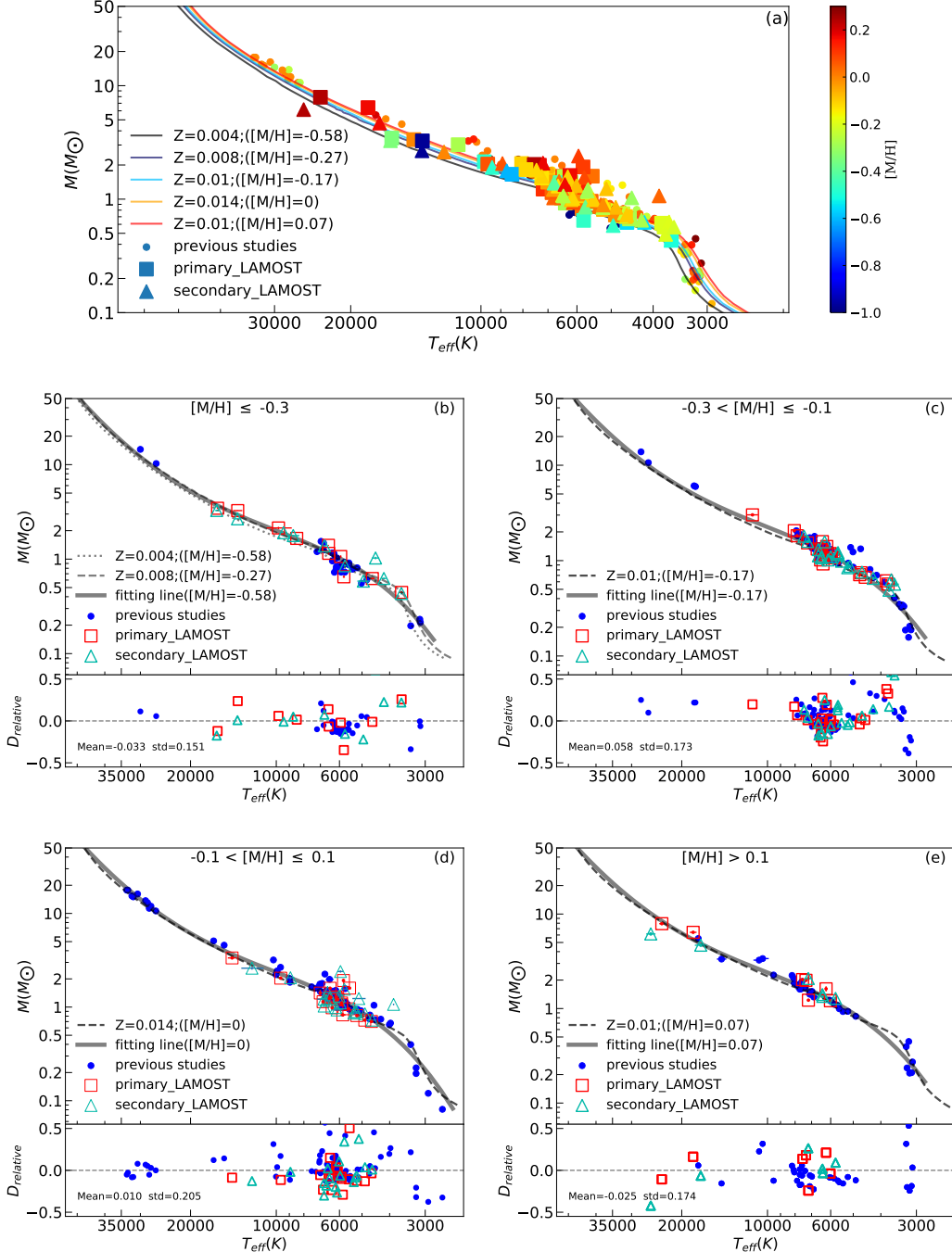


Figure 5. The $T_{\text{eff}}-M$ diagram. Panel (a) shows the total samples with various metallicity. The solid lines stand for the ZAMS with color-coded $[\text{M}/\text{H}]$ from PARSEC, while the dots are the samples compiled from the literature. The rectangles and triangles are the primary and secondary stars, respectively, from LAMOST MRS. Panels (b)-(e) show the $T_{\text{eff}}-M$ diagrams for the stars with different range of $[\text{M}/\text{H}]$. The theoretical ZAMS lines from PARSEC are shown as black dashed lines in the panels. The blue dots, red hollow rectangles, and cyan hollow triangles indicate the stars from literature, the primary and secondary stars from LAMOST MRS, respectively. The parameters of the secondary stars are estimated from PHOEBE. The thick solid gray lines display the best-fit quartic polynomial of M as a function of T_{eff} and $[\text{M}/\text{H}]$. At the bottom of each panels (b)-(e), the relative residuals, defined as $D_{\text{relative}} = (M_{\text{obs}} - M_{\text{poly}})/M_{\text{poly}}$ in which M_{obs} and M_{poly} are masses from observation and polynomial model respectively, are illustrated.

panel (a) are mostly located above the ZAMS lines. The gradient of metallicity in the $T_{\text{eff}}-R$ plane is not seen in

the stellar samples since that R is either affected by age or by uncertainties of the R and T_{eff} estimates.

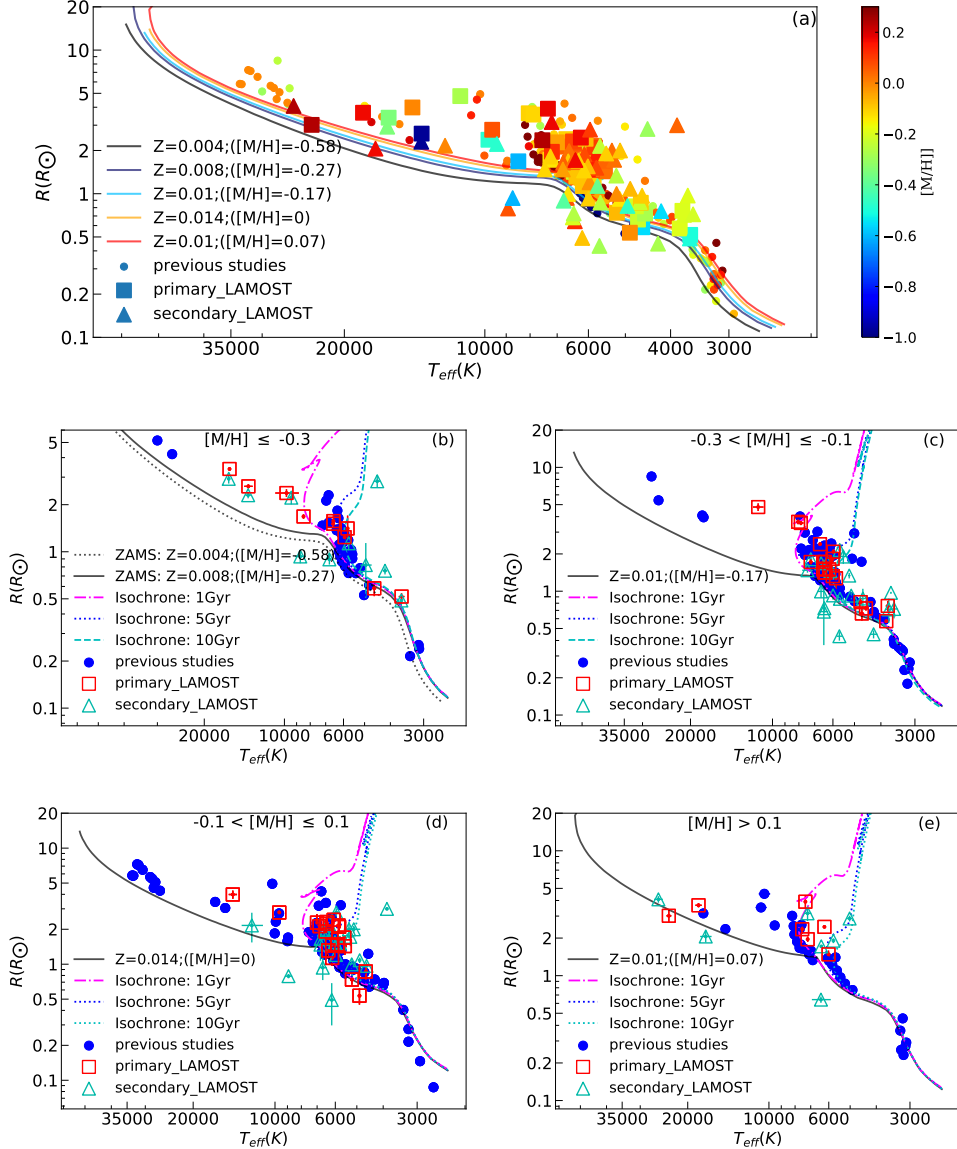


Figure 6. The T_{eff} - R diagram. Panel (a) shows the overall distribution of all samples using dots (known stars from literature), rectangles (primary of the new samples from LAMOST), and triangles (secondary stars from LAMOST). The solid lines indicate the ZAMS lines with color-coded $[M/H]$ from PARSEC. The dots also with color-coded $[M/H]$ are the samples compiled from the literature and the rectangles are the samples selected from LAMOST MRS. Panel (b) shows the T_{eff} - R diagram with $[M/H] < -0.3$, in which the blue filled circles, red hollow rectangles, and cyan hollow triangles are same as in Figure 5 (b)-(e). The black solid and dashed lines are the ZAMS lines from PARSEC from $Z = 0.008$ and 0.004 , respectively. The magenta dot-dashed, blue dotted and cyan dashed lines stand for three isochrones with age of 1, 5, and 10 Gyr, respectively, at $Z = 0.008$. Panels (c)-(e) are similar to panel (b), but at different metallicities.

In panels (b)-(e), the T_{eff} - R relations with different ranges of $[M/H]$ are displayed, respectively. The solid lines indicate the ZAMS lines at different $[M/H]$, while dot-dashed, dotted, and dashed lines with color-coded ages are the isochrones with the ages of 1, 5, and 10 Gyr, respectively. The influence of age, which moves older stars upward out of ZAMS, especially near $T_{\text{eff}} \sim 6000$ K, is clearly seen in all the panels. Comparing to the theoretical isochrones, it implies that, with accurate

measurement of radius and effective temperature, one would also determine the age of stars, not only for turn-off stars (which is one of the most sensitive kinds), but also for stars at a large range of T_{eff} .

In panel (d), for the stars with $T_{\text{eff}} < 4000$ K, as seen in figure 4 (c), a clear deviation between the observed stars and the theoretical ZAMS is found. This may be caused by the inaccurate atmospheric model for cool stars.

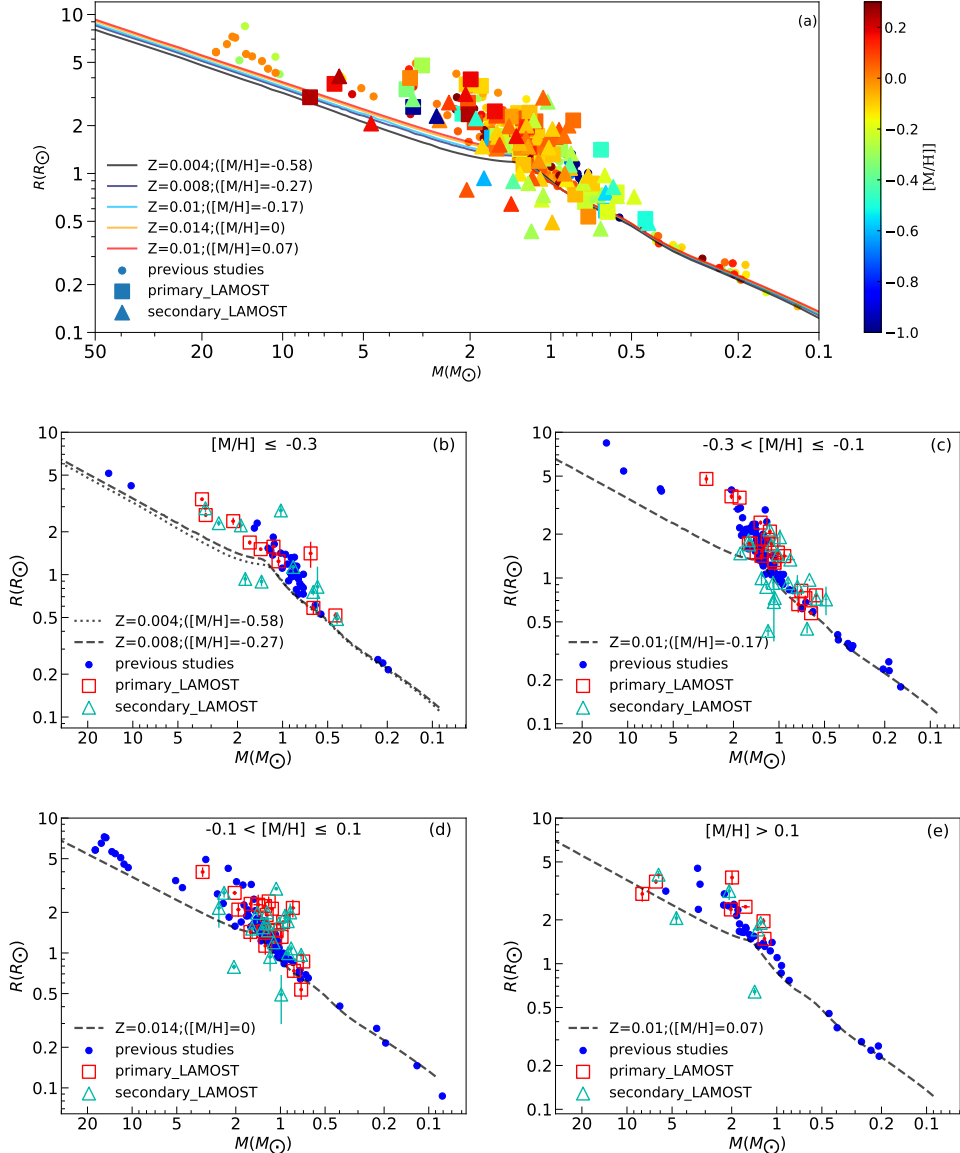


Figure 7. The mass-radius diagram. Panel (a) shows the overall M - R distribution of the samples including both the compiled (dots with color-coded metallicities)) and LAMOST data (rectangles and triangles represent for the primary and secondary stars, respectively). The solid lines with color-coded metallicities are the ZAMS lines with from PARSEC. Panels (b)-(e) display the M - R relations in different ranges of $[M/H]$. The dotted or dashed lines indicate ZAMS lines with similar metallicity. The symbols are same as in Figure 5 (b)-(e).

4.1.3. M - R relations in different ranges of $[M/H]$

Figure 7 shows the M - R relations of our samples including both compiled and LAMOST MRS data. In principle, the trend is quite consistent with that presented by Eker et al. (2018). In panel (a), the ZAMS lines show that the difference of M - R relations in different $[M/H]$ is small, at least in the range of $-0.58 < [M/H] < +0.07$. In particular, when $M < 0.5$, the ZAMS lines with different $[M/H]$ are almost overlapped with the observed data.

Panels (b)-(e) separately show the M - R relations in different ranges of $[M/H]$. Compared to the T_{eff} - R relations, they display that the M - R relation of the observed samples are well consistent with the stellar models, especially at $M < 1 M_\odot$, in different ranges of $[M/H]$.

Almost all the data samples are located on above the theoretical ZAMS lines. Although the stellar masses does not significantly change from ZAMS, their radii enlarge to the extent that we are able to measure. In particular, for the stars with mass around $2 M_\odot$, the radii can extend to a factor of a few from the initial

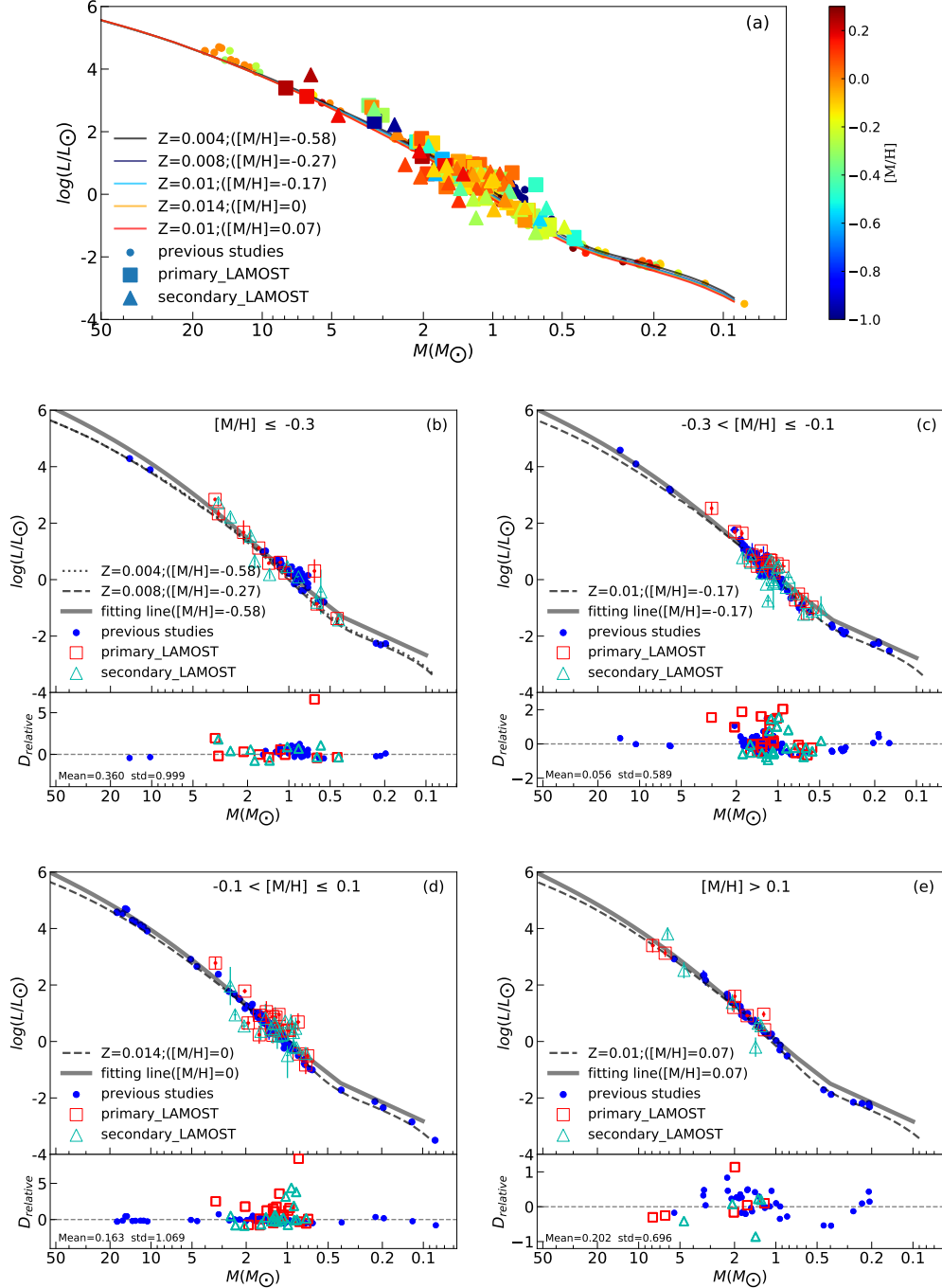


Figure 8. Panel (a) displays the M - L diagram. The solid lines with different colors are the ZAMS lines with color-coded $[M/H]$ from PARSEC. The dots, rectangles, and triangles stand for the stars from literature, the primary and secondary stars from LAMOST MRS, respectively. The colors of the symbols are same as those of the ZAMS lines. Panels (b)-(e) show the M - L diagrams with different range of $[M/H]$. The dash lines are the ZAMS lines from PARSEC. The thick solid lines are the best-fit polynomial model. The other symbols are same as in Figure 5 (b)-(e).

value at ZAMS with same mass. The explanations of the phenomenon are mainly considered as the evolution of stars (Torres et al. 2010), ages, rotation (Irwin et al. 2011; Kraus et al. 2011), and magnetic fields (Spruit

& Weiss 1986; Feiden & Chaboyer 2012; MacDonald & Mullan 2013).

4.1.4. M - L diagrams in different ranges of $[M/H]$

The luminosity, which is defined as $L = 4\pi R^2 \cdot \sigma T_{eff}^4$, is derived from T_{eff} and R . As logarithmic form, $\log L =$

$4 \log T_{\text{eff}} + 2 \log R - 15.045$, in which L , R are in units of the Sun.

Figure 8 shows the M - L diagram. In panel (a), the color-coded solid lines are the ZAMS lines with different [M/H], the dots are stars from literature, and the rectangles are those from LAMOST MRS. Colors of these symbols represent for the metallicity with same code as the ZAMS lines. It is seen that [M/H] is almost independent in the M - L relation, which is consistent with the stellar model showing in ZAMS lines. Furthermore, at around $1 M_{\odot}$, a larger dispersion in observed data can be clearly seen in the panel. This is likely due to the influence of age.

The M - L diagrams with different [M/H] are shown in panels (b)-(e). It shows that, at each metallicity bin, the observed data are all well consistent with the stellar models. It is noted that at low mass end with $M < 1 M_{\odot}$, unlike the T_{eff} - M and T_{eff} - R relations, the data also well agree with the models. This means that, although R is not well predicted by stellar model for low mass stars, the luminosity predicted by model seems quite good.

We also conducted an polynomial model of M - L -[M/H] relation and find the best-fit coefficients of the model using the stellar samples. The following relationship also only apply for the unevolved stars. The polynomial model is written as:

$$\begin{aligned} \log(L) = & a_1 + a_2 \log(M) + a_3 \log(M)^2 \\ & - 0.755 \log(M)^3 + 0.189 \log(M)^4 + a_4 Z, \end{aligned} \quad (5)$$

in which, a_1 , a_2 , a_3 , a_4 are 0.066, 4.141, 0.314, -0.245, respectively. The coefficients of the 3rd and 4th order terms of $\log M$ are determined from the polynomial fitting to the model. The best-fit M - L polynomial model is shown as thick solid lines for different [M/H] in panels (b)-(e), respectively. The relative difference between observed data and model (L_{fit}), $D_{\text{relative}} = (L - L_{\text{fit}})/L_{\text{fit}}$, is shown in the bottom of each panel.

5. DISCUSSION

The high-precision, model-independent mass and radius derived from binaries allow us to calibrate different methods of estimation of mass and radius for single stars from observational atmospheric parameters (e.g. T_{eff} , $\log g$ and [M/H]).

In this section, we compare the M and R derived from orbital solutions with those from other measurements.

There are lots of approaches to obtain stellar mass and radius. Figure 9 summarizes the usual paths to the two parameters.

In principle, there are three kinds of approaches, which are drawn as three rectangles in the second layer, to estimate M and R .

Each approach requires observed parameters drawn in the third layer in figure 9. The solid blocks indicate the parameters directly obtained from observation and the dotted blocks are the parameters derived from some known relationships, which are shown in the green circles with dotted lines.

Other than orbital solution, the stellar mass can also be determined using isochrone fitting with T_{eff} , $\log g$, and metallicity as inputs. Luminosity can also be used in the isochrone fitting for the stellar mass. In total, there are three usual methods for mass estimation: orbital solution, isochrone fitting with T_{eff} , $\log g$, and Z , and isochrone fitting with additional $\log L$ derived either from parallax. These 3 methods are listed in Table 4.

To estimate the stellar radius, one usually have four other methods than the orbital solution. The first two use isochrone fitting with or without luminosity. The luminosity required in radius estimation should be determined from parallax. The other two methods are based on SED fitting either with multi-band photometry, T_{eff} , and distance or with additional mass ratio, q from other methods.

Table 4 summarizes all these methods with different input parameters and the results of the comparison with binary orbital solution. We compare the results of mass and radius from various methods and assess the performance of them based on the results from the orbital solutions.

In general, all isochrone fitting approaches have similar process, that is, to find the best-fit physical parameters in synthetic stellar models with most similar observed atmospheric parameters and/or luminosity.

In this study, Nearest Neighbor Search (NNS) is applied to find the best-match stellar atmospheric parameters and/or luminosity in the PARSEC (Bressan et al. 2012) theoretical stellar model grid. The atmospheric parameters and/or luminosity to be matched are defined as a vector $\theta = (T_{\text{eff}}, \log g, [\text{M}/\text{H}])$ or $(T_{\text{eff}}, \log g, [\text{M}/\text{H}], L)$, in which L is derived from parallax. The PARSEC isochrone grid with [M/H] in (-2.0 dex \sim +0.5 dex) and ages in (10 Myr \sim 10 Gyr) sets up the search space $S = \{s_1, s_2, s_3, \dots, s_n\}$ with various combination of T_{eff} , $\log g$, and [M/H]. Firstly, we generate a searching point (θ_{th}) following a uniform distribution within the range of ± 3 times measurement errors for θ . Second, the distance between PARSEC isochrone grid and θ_{th} is calculated such that

$$d(\theta_{th,i}, s_{n,i}) = \sqrt{\sum_{i=1}^m ((s_{n,i} - \theta_{th,i})/C_i)^2}, \quad (6)$$

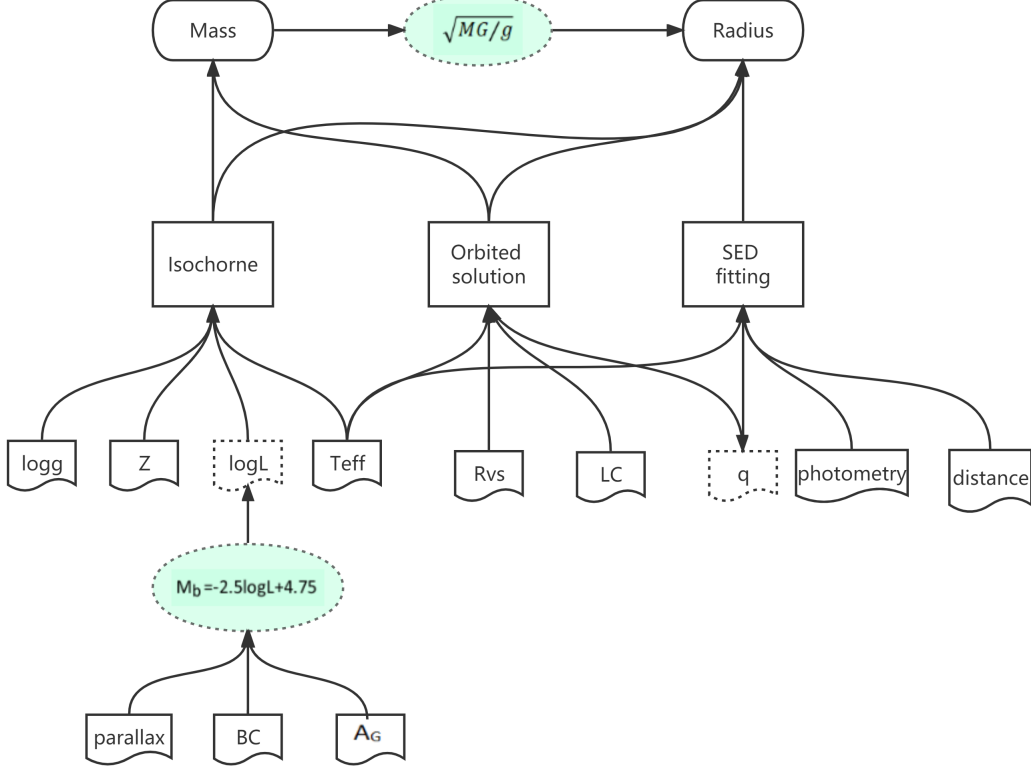


Figure 9. Summary of parameter measurement approaches. The rectangles in the second layer are measurements for mass and radius. In the third layer, the solid blocks are the parameters directly obtained from observation and the dotted blocks are the parameters derived from some relations. The green circles are relationships between parameters.

Table 4. Summary of the usual mass and radius measurement methods.

Parameters	Definition	Method	Input Parameters	Mean relative difference ^a	Random error
	M	Orbited solution	RVs(RV ₁ and RV ₂), LC, T _{eff} (primary star);	-	-
	M _g	Isochorne fitting	T _{eff} , log g, [M/H]	0.010	0.143
	M _{LG}	Isochorne fitting	T _{eff} , log g, [M/H]; logL;	-0.289	0.188
Radius	R	Orbited solution	RVs(RV ₁ and RV ₂), LC, T _{eff} (primary star);	-	-
	R _g	Isochorne fitting	T _{eff} , log g, [M/H];	0.011	0.164
	R _{LG}	Isochorne fitting	T _{eff} , log g, [M/H], log L;	-0.322	0.191
	R _{SED}	SED fitting	T _{eff} (T ₁ and T ₂), q, distance and photometry from Gaia;	-0.029	0.205
	R _{Mg}	$\sqrt{MG/g}$	mass, log g ;	0.027	0.292

^a relative difference: $(M - M_X) / M_X$, X are various methods

where i represents T_{eff} , $\log g$, $[\text{M}/\text{H}]$ or with additional L and $m = 3$ or 4 depending whether luminosity is among the input parameters. C is a custom coefficient to unify the parameters scale. We empirically adopt C as 1000 for T_{eff} , 0.25 for $\log g$ and L , and 0.1 for $[\text{M}/\text{H}]$. Third, we search for the closest point to θ in S and adopt the mass and radius of the nearest neighbor point as the best estimates. Finally, we obtain the mass and radius estimation with measurement error by repeating the above steps 5000 times. In each time, the input θ are randomly drawn from a Gaussian distribution adopting the uncertainties of θ as scales. During this process, T_{eff} , $\log g$,

and $[\text{M}/\text{H}]$ are obtained from the observed spectra. L is measured using the bolometric magnitude, which is

$$\log L = 0.45(M_{b,\odot} - M_b), \quad (7)$$

where $M_{b,\odot}$ is the absolute bolometric magnitude of the Sun. The absolute bolometric magnitude M_b of each star is derived from

$$M_b = M'_G - A_G + BC_G, \quad (8)$$

where M'_G is derived by the following equation (Gaia Collaboration et al. 2018):

$$M'_G = G + 5 + 5 \log_{10}(\varpi/1000) \quad (9)$$

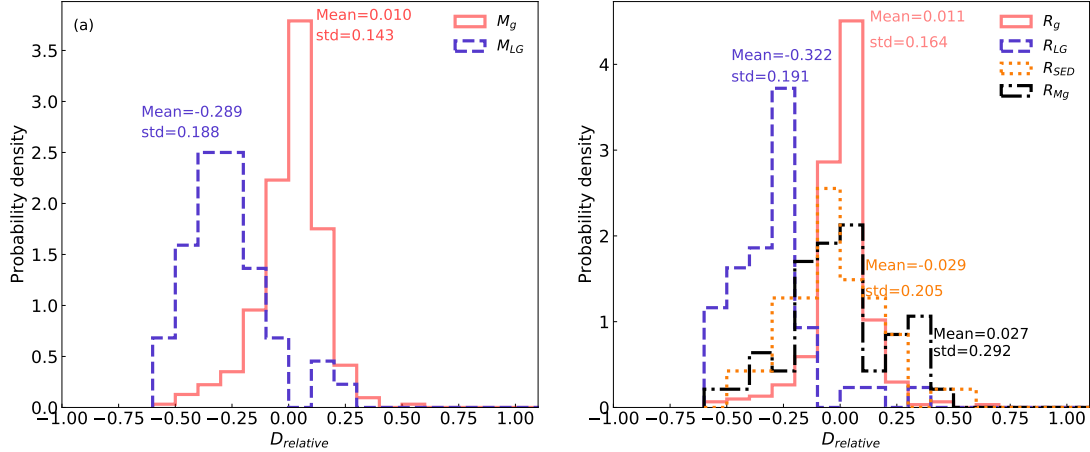


Figure 10. Panel (a) shows the histogram of the relative residuals ($D_{relative} = (M_x - M)/M$, where x represents either g or LG) between dynamic mass (M) and the mass derived from model or relations. Panel (b) shows the histogram of the relative residuals ($D_{relative} = (R_x - R)/R$, where x stands for g , LG , SED , or Mg) between dynamic radius (R) and the radius derived from model or relations.

based on photometric and astrometric data of Gaia EDR3 (Gaia Collaboration et al. 2020). In Eq. 9, G is G magnitude, ϖ is the parallax in milli-arcsecond. The extinction A_V is given from the 3-D dust map provided by *dustmaps bayestar* (Green et al. 2019). A_G is further derived from A_V using the extinction coefficient from Wang & Chen (2019). Finally, the bolometric correction of stars are obtained from Chen et al. (2019).

In figure 10, panel (a) shows the histogram of the relative residuals between dynamical mass (M) and other mass estimates. And panel (b) displays the histogram of the relative residuals between dynamical radius and other radius estimates.

It is seen from the red line that, with T_{eff} , $\log g$, and $[M/H]$, the stellar mass estimated from isochrone fitting can reach random error of about 14.3%. The systematic bias in M_g is only 1.0%, which is quite small. This implies that the stellar model applied in the isochrone is quite accurate compared to the dynamical mass.

The blue dashed line shows the performance of M_{LG} estimates, which is derived from isochrone fitting of the LAMOST MRS samples with $RUWE < 1.5$. The luminosities are estimated based on *Gaia* parallax. The relative systematic bias of M_{LG} is -28.9%, which is slightly larger compared to the random error, which is 18.8%.

It seems that the isochrone fitting without luminosity can well reproduce stellar mass, while with luminosity, it tends to overestimate stellar mass. The systematic bias and larger random error of M_{LG} is probably due to the large uncertainties of bolometric correction in G -band.

Panel (b) shows the difference between dynamical radius (R) and the those derived from other 4 methods. The red solid line shows that the isochrone derived ra-

dius R_g using T_{eff} , $\log g$, and $[M/H]$ as inputs tightly follows the dynamical radius. The systematic difference between R_g and R is only 1.1% with random error of 16.4%.

The blue dashed line shows the comparison between dynamical R and R_{LG} , which is obtained from isochrone fitting using T_{eff} , $\log g$, $[M/H]$, and L . Similar to the mass estimate M_{LG} , a significant overestimation of 32.2% occurs in R_{LG} . This is again likely cause by the larger uncertainty of bolometric correction.

The orange dotted line shows that the SED derived radius R_{SED} is quite consistent with the dynamical values. The mean difference is only -2.9% with random error of 20.5%. The surface gravity-derived radius R_{Mg} shows similar performance as seen in the black dot-dashed line. The bias is 2.7% and the random error is 29.2%, slightly larger than that for R_{SED} . Note that R_{SED} adopts accurate distance derived from parallax given by *Gaia* and R_{Mg} uses dynamical mass in the calculation. These accurate parameters are helpful to constrain the accuracy of R_{SED} and R_{Mg} .

The accuracy of atmospheric stellar parameters T_{eff} , $\log g$, $[M/H]$, and L are critical in the precision of mass and radii estimation from the stellar model. If these parameters can not be measured in high-precision, the mass and radius can not be accurately constrained.

6. CONCLUSIONS

In this work, we publish 56 new detached binaries selected from LAMOST MRS survey combined with 128 detached eclipsing binaries with independent atmospheric parameters (T_{eff} , $\log g$, $[M/H]$) and accurate masses and radii compiled from previous studies. For the 56 LAMOST observed detached binaries, we per-

form the MCMC method with PHOEBE to obtain the orbital solutions. With the additional LAMOST stars, we are able to increase the samples at each [M/H] bin. In particular, we extend the samples to lower [M/H] for high T_{eff} stars. Hence, the distribution of [M/H] and T_{eff} becomes more continuous and densified. In total, we provide a catalog containing 128 binaries as the benchmark of stellar mass and radius covering a wide range of stellar parameters. The measurement uncertainties of masses and radii are within 5%.

We compared the samples with PARSEC model in different [M/H] and found that the observed data, including the new 56 LAMOST stars and the 128 stars from literature, essentially well match with the PARSEC isochrones. In addition, we also find that the enlarged radii at around the turn-off point depend more on stellar ages than rotational velocity. Therefore, the radius estimates of the turn-off stars can also be potentially used as an indicator of age.

The comparisons between dynamical masses and radii with those derived from the stellar models show that the precision of model-estimated mass is >10% and that of model-estimated radius is >15% based on atmospheric parameters.

This work is supported by the National Key R&D Program of China No. 2019YFA0405500. C.L. Thanks the National Natural Science Foundation of China (NSFC) with grant Nos.11835057, 12173047, 12073047. The Guoshoujing Telescope (the Large Sky Area Multi-Object Fiber Spectroscopic Telescope LAMOST) is a National Major Scientific Project built by the Chinese Academy of Sciences. Funding for the project has been provided by the National Development and Reform Commission. LAMOST is operated and managed by the National Astronomical Observatories, Chinese Academy of Sciences.

REFERENCES

- Abdul-Masih, M., Prša, A., Conroy, K., et al. 2016, AJ, 151, 101, doi: [10.3847/0004-6256/151/4/101](https://doi.org/10.3847/0004-6256/151/4/101)
- Andersen, J., Clausen, J. V., Nordstrom, B., Gustafsson, B., & Vandenberg, D. A. 1988, A&A, 196, 128
- Batalha, N. M., Borucki, W. J., Koch, D. G., et al. 2010, ApJL, 713, L109, doi: [10.1088/2041-8205/713/2/L109](https://doi.org/10.1088/2041-8205/713/2/L109)
- Bellm, E. C., Kulkarni, S. R., Graham, M. J., et al. 2019, PASP, 131, 018002, doi: [10.1088/1538-3873/aaecbe](https://doi.org/10.1088/1538-3873/aaecbe)
- Borucki, W. J., Koch, D., Basri, G., et al. 2010, Science, 327, 977, doi: [10.1126/science.1185402](https://doi.org/10.1126/science.1185402)
- Bressan, A., Marigo, P., Girardi, L., et al. 2012, MNRAS, 427, 127, doi: [10.1111/j.1365-2966.2012.21948.x](https://doi.org/10.1111/j.1365-2966.2012.21948.x)
- Brogaard, K., VandenBerg, D. A., Bedin, L. R., et al. 2017, MNRAS, 468, 645, doi: [10.1093/mnras/stx378](https://doi.org/10.1093/mnras/stx378)
- Chaplin, W. J., Basu, S., Huber, D., et al. 2014, ApJS, 210, 1, doi: [10.1088/0067-0049/210/1/1](https://doi.org/10.1088/0067-0049/210/1/1)
- Chen, X., Wang, S., Deng, L., et al. 2020, ApJS, 249, 18, doi: [10.3847/1538-4365/ab9cae](https://doi.org/10.3847/1538-4365/ab9cae)
- Chen, Y., Girardi, L., Fu, X., et al. 2019, A&A, 632, A105, doi: [10.1051/0004-6361/201936612](https://doi.org/10.1051/0004-6361/201936612)
- Clausen, J. V., Torres, G., Bruntt, H., et al. 2008, A&A, 487, 1095, doi: [10.1051/0004-6361:200809671](https://doi.org/10.1051/0004-6361:200809671)
- Cox, A. N. 2000, Allen's astrophysical quantities
- Cropper, M., Katz, D., Sartoretti, P., et al. 2018, A&A, 616, A5, doi: [10.1051/0004-6361/201832763](https://doi.org/10.1051/0004-6361/201832763)
- Cui, X.-Q., Zhao, Y.-H., Chu, Y.-Q., et al. 2012, Research in Astronomy and Astrophysics, 12, 1197, doi: [10.1088/1674-4527/12/9/003](https://doi.org/10.1088/1674-4527/12/9/003)
- De Silva, G. M., Freeman, K. C., Bland-Hawthorn, J., et al. 2015, MNRAS, 449, 2604, doi: [10.1093/mnras/stv327](https://doi.org/10.1093/mnras/stv327)
- Demarque, P., Guenther, D. B., Li, L. H., Mazumdar, A., & Straka, C. W. 2008, Ap&SS, 316, 31, doi: [10.1007/s10509-007-9698-y](https://doi.org/10.1007/s10509-007-9698-y)
- Demarque, P., Woo, J.-H., Kim, Y.-C., & Yi, S. K. 2004, ApJS, 155, 667, doi: [10.1086/424966](https://doi.org/10.1086/424966)
- Deng, L.-C., Newberg, H. J., Liu, C., et al. 2012, Research in Astronomy and Astrophysics, 12, 735, doi: [10.1088/1674-4527/12/7/003](https://doi.org/10.1088/1674-4527/12/7/003)
- Dieterich, S. B., Simler, A., Henry, T. J., & Jao, W.-C. 2021, AJ, 161, 172, doi: [10.3847/1538-3881/abd2c2](https://doi.org/10.3847/1538-3881/abd2c2)
- Dotter, A. 2016, ApJS, 222, 8, doi: [10.3847/0067-0049/222/1/8](https://doi.org/10.3847/0067-0049/222/1/8)
- Dotter, A., Chaboyer, B., Jevremović, D., et al. 2008, ApJS, 178, 89, doi: [10.1086/589654](https://doi.org/10.1086/589654)
- Eker, Z., Bilir, S., Soydugan, F., et al. 2014, PASA, 31, e024, doi: [10.1017/pasa.2014.17](https://doi.org/10.1017/pasa.2014.17)
- Eker, Z., Soydugan, F., Soydugan, E., et al. 2015, AJ, 149, 131, doi: [10.1088/0004-6256/149/4/131](https://doi.org/10.1088/0004-6256/149/4/131)
- Eker, Z., Bakış, V., Bilir, S., et al. 2018, MNRAS, 479, 5491, doi: [10.1093/mnras/sty1834](https://doi.org/10.1093/mnras/sty1834)
- El-Badry, K., Rix, H.-W., Ting, Y.-S., et al. 2018, MNRAS, 473, 5043, doi: [10.1093/mnras/stx2758](https://doi.org/10.1093/mnras/stx2758)
- Feiden, G. A., & Chaboyer, B. 2012, ApJ, 757, 42, doi: [10.1088/0004-637X/757/1/42](https://doi.org/10.1088/0004-637X/757/1/42)
- Foreman-Mackey, D., Hogg, D. W., Lang, D., & Goodman, J. 2013, PASP, 125, 306, doi: [10.1086/670067](https://doi.org/10.1086/670067)

- Gaia Collaboration, Brown, A. G. A., Vallenari, A., et al. 2020, arXiv e-prints, arXiv:2012.01533.
<https://arxiv.org/abs/2012.01533>
- Gaia Collaboration, Babusiaux, C., van Leeuwen, F., et al. 2018, *A&A*, 616, A10, doi: [10.1051/0004-6361/201832843](https://doi.org/10.1051/0004-6361/201832843)
- Gallenne, A., Pietrzyński, G., Graczyk, D., et al. 2019, *A&A*, 632, A31, doi: [10.1051/0004-6361/201935837](https://doi.org/10.1051/0004-6361/201935837)
- Gilmore, G., Randich, S., Asplund, M., et al. 2012, *The Messenger*, 147, 25
- Graczyk, D., Pietrzyński, G., Galan, C., et al. 2021, *A&A*, 649, A109, doi: [10.1051/0004-6361/202140571](https://doi.org/10.1051/0004-6361/202140571)
- Green, G. M., Schlafly, E., Zucker, C., Speagle, J. S., & Finkbeiner, D. 2019, *ApJ*, 887, 93, doi: [10.3847/1538-4357/ab5362](https://doi.org/10.3847/1538-4357/ab5362)
- Guo, Y., Zhang, B., Liu, C., et al. 2021, *ApJS*, 257, 54, doi: [10.3847/1538-4365/ac2ded](https://doi.org/10.3847/1538-4365/ac2ded)
- Hełminiak, K. G., Moharana, A., Pawar, T., et al. 2021, *MNRAS*, 508, 5687, doi: [10.1093/mnras/stab2963](https://doi.org/10.1093/mnras/stab2963)
- Hoxie, D. T. 1973, *A&A*, 26, 437
- Irwin, J. M., Quinn, S. N., Berta, Z. K., et al. 2011, *ApJ*, 742, 123, doi: [10.1088/0004-637X/742/2/123](https://doi.org/10.1088/0004-637X/742/2/123)
- Jayasinghe, T., Stanek, K. Z., Kochanek, C. S., et al. 2019, *MNRAS*, 485, 961, doi: [10.1093/mnras/stz444](https://doi.org/10.1093/mnras/stz444)
- . 2020, *MNRAS*, 491, 13, doi: [10.1093/mnras/stz2711](https://doi.org/10.1093/mnras/stz2711)
- Jayasinghe, T., Kochanek, C. S., Stanek, K. Z., et al. 2021, *MNRAS*, 503, 200, doi: [10.1093/mnras/stab114](https://doi.org/10.1093/mnras/stab114)
- Jones, D., Conroy, K. E., Horvat, M., et al. 2020, *ApJS*, 247, 63, doi: [10.3847/1538-4365/ab7927](https://doi.org/10.3847/1538-4365/ab7927)
- Katz, D., Munari, U., Cropper, M., et al. 2004, *MNRAS*, 354, 1223, doi: [10.1111/j.1365-2966.2004.08282.x](https://doi.org/10.1111/j.1365-2966.2004.08282.x)
- Kjurkchieva, D., & Vasileva, D. 2015, *PASA*, 32, e023, doi: [10.1017/pasa.2015.23](https://doi.org/10.1017/pasa.2015.23)
- Kochanek, C. S., Shappee, B. J., Stanek, K. Z., et al. 2017, *PASP*, 129, 104502, doi: [10.1088/1538-3873/aa80d9](https://doi.org/10.1088/1538-3873/aa80d9)
- Kraus, A. L., Tucker, R. A., Thompson, M. I., Craine, E. R., & Hillenbrand, L. A. 2011, *ApJ*, 728, 48, doi: [10.1088/0004-637X/728/1/48](https://doi.org/10.1088/0004-637X/728/1/48)
- Li, C.-q., Shi, J.-r., Yan, H.-l., et al. 2021a, *ApJS*, 256, 31, doi: [10.3847/1538-4365/ac22a8](https://doi.org/10.3847/1538-4365/ac22a8)
- Li, J., Liu, C., Zhang, B., et al. 2021b, *ApJS*, 253, 45, doi: [10.3847/1538-4365/abelc1](https://doi.org/10.3847/1538-4365/abelc1)
- Liu, C., Fu, J., Shi, J., et al. 2020, arXiv e-prints, arXiv:2005.07210. <https://arxiv.org/abs/2005.07210>
- Luo, A. L., Zhao, Y.-H., Zhao, G., et al. 2015, *Research in Astronomy and Astrophysics*, 15, 1095, doi: [10.1088/1674-4527/15/8/002](https://doi.org/10.1088/1674-4527/15/8/002)
- MacDonald, J., & Mullan, D. J. 2013, *ApJ*, 765, 126, doi: [10.1088/0004-637X/765/2/126](https://doi.org/10.1088/0004-637X/765/2/126)
- Majewski, S. R., Schiavon, R. P., Frinchaboy, P. M., et al. 2017, *AJ*, 154, 94, doi: [10.3847/1538-3881/aa784d](https://doi.org/10.3847/1538-3881/aa784d)
- Marcy, G. W., Isaacson, H., Howard, A. W., et al. 2014, *ApJS*, 210, 20, doi: [10.1088/0067-0049/210/2/20](https://doi.org/10.1088/0067-0049/210/2/20)
- Miller, N. J., Maxted, P. F. L., Graczyk, D., Tan, T. G., & Southworth, J. 2022, *MNRAS*, doi: [10.1093/mnras/stac2968](https://doi.org/10.1093/mnras/stac2968)
- Pan, Y., Fu, J.-N., Zong, W., et al. 2020, *The Astrophysical Journal*, 905, 67, doi: [10.3847/1538-4357/abc250](https://doi.org/10.3847/1538-4357/abc250)
- Pavlovski, K., Southworth, J., & Tamajo, E. 2018, *MNRAS*, 481, 3129, doi: [10.1093/mnras/sty2516](https://doi.org/10.1093/mnras/sty2516)
- Popper, D. M., & Hill, G. 1991, *AJ*, 101, 600, doi: [10.1086/115709](https://doi.org/10.1086/115709)
- Prša, A., & Zwitter, T. 2005, *ApJ*, 628, 426, doi: [10.1086/430591](https://doi.org/10.1086/430591)
- Prša, A., Batalha, N., Slawson, R. W., et al. 2011, *AJ*, 141, 83, doi: [10.1088/0004-6256/141/3/83](https://doi.org/10.1088/0004-6256/141/3/83)
- Prša, A., Conroy, K. E., Horvat, M., et al. 2016, *ApJS*, 227, 29, doi: [10.3847/1538-4365/227/2/29](https://doi.org/10.3847/1538-4365/227/2/29)
- Ricker, G. R., Winn, J. N., Vandervspek, R., et al. 2015, *Journal of Astronomical Telescopes, Instruments, and Systems*, 1, 014003, doi: [10.1117/1.JATIS.1.1.014003](https://doi.org/10.1117/1.JATIS.1.1.014003)
- Serenelli, A., Weiss, A., Aerts, C., et al. 2021, *A&A Rv*, 29, 4, doi: [10.1007/s00159-021-00132-9](https://doi.org/10.1007/s00159-021-00132-9)
- Slawson, R. W., Prša, A., Welsh, W. F., et al. 2011, *AJ*, 142, 160, doi: [10.1088/0004-6256/142/5/160](https://doi.org/10.1088/0004-6256/142/5/160)
- Southworth, J. 2015, in *Astronomical Society of the Pacific Conference Series*, Vol. 496, *Living Together: Planets, Host Stars and Binaries*, ed. S. M. Rucinski, G. Torres, & M. Zejda, 164. <https://arxiv.org/abs/1411.1219>
- Spruit, H. C., & Weiss, A. 1986, *A&A*, 166, 167
- Steinmetz, M., Zwitter, T., Siebert, A., et al. 2006, *AJ*, 132, 1645, doi: [10.1086/506564](https://doi.org/10.1086/506564)
- Steinmetz, M., Guiglion, G., McMillan, P. J., et al. 2020, *AJ*, 160, 83, doi: [10.3847/1538-3881/ab9ab8](https://doi.org/10.3847/1538-3881/ab9ab8)
- Stempels, H. C., Hebb, L., Stassun, K. G., et al. 2008, *A&A*, 481, 747, doi: [10.1051/0004-6361:20078585](https://doi.org/10.1051/0004-6361:20078585)
- Thompson, I. B., Udalski, A., Dotter, A., et al. 2020, *MNRAS*, 492, 4254, doi: [10.1093/mnras/staa032](https://doi.org/10.1093/mnras/staa032)
- Torres, G., Andersen, J., & Giménez, A. 2010, *A&A Rv*, 18, 67, doi: [10.1007/s00159-009-0025-1](https://doi.org/10.1007/s00159-009-0025-1)
- Wang, J., Fu, J., Niu, H., et al. 2021, *MNRAS*, 504, 4302, doi: [10.1093/mnras/stab1219](https://doi.org/10.1093/mnras/stab1219)
- Wang, R., Luo, A. L., Chen, J. J., et al. 2019, *ApJS*, 244, 27, doi: [10.3847/1538-4365/ab3cc0](https://doi.org/10.3847/1538-4365/ab3cc0)
- Wang, R., Luo, A. L., Chen, J.-J., et al. 2020, *ApJ*, 891, 23, doi: [10.3847/1538-4357/ab6dea](https://doi.org/10.3847/1538-4357/ab6dea)
- Wang, S., & Chen, X. 2019, *ApJ*, 877, 116, doi: [10.3847/1538-4357/ab1c61](https://doi.org/10.3847/1538-4357/ab1c61)
- Wilson, R. E., & Devinney, E. J. 1971, *ApJ*, 166, 605, doi: [10.1086/150986](https://doi.org/10.1086/150986)

- Wu, Y., Du, B., Luo, A., Zhao, Y., & Yuan, H. 2014, in Statistical Challenges in 21st Century Cosmology, ed. A. Heavens, J.-L. Starck, & A. Krone-Martins, Vol. 306, 340–342, doi: [10.1017/S1743921314010825](https://doi.org/10.1017/S1743921314010825)
- Xiang, M. S., Liu, X. W., Yuan, H. B., et al. 2015, MNRAS, 448, 822, doi: [10.1093/mnras/stu2692](https://doi.org/10.1093/mnras/stu2692)
- Xiong, J.-P., Zhang, B., Liu, C., et al. 2021, Research in Astronomy and Astrophysics, 21, 265, doi: [10.1088/1674-4527/21/10/265](https://doi.org/10.1088/1674-4527/21/10/265)
- Yanny, B., Rockosi, C., Newberg, H. J., et al. 2009, AJ, 137, 4377, doi: [10.1088/0004-6256/137/5/4377](https://doi.org/10.1088/0004-6256/137/5/4377)
- Zhang, B., Li, J., Yang, F., et al. 2021, ApJS, 256, 14, doi: [10.3847/1538-4365/ac0834](https://doi.org/10.3847/1538-4365/ac0834)
- Zhang, B., Jing, Y.-J., Yang, F., et al. 2022, ApJS, 258, 26, doi: [10.3847/1538-4365/ac42d1](https://doi.org/10.3847/1538-4365/ac42d1)
- Zhao, G., Zhao, Y.-H., Chu, Y.-Q., Jing, Y.-P., & Deng, L.-C. 2012, Research in Astronomy and Astrophysics, 12, 723, doi: [10.1088/1674-4527/12/7/002](https://doi.org/10.1088/1674-4527/12/7/002)